Delgado-Muñoz, D.; Chieregato, A.; Soriano Rodríguez, MD.; Rodríguez-Aguado, E.; Ruiz-Rodríguez, L.; Rodriguez-Castellon, E.; López Nieto, JM. (14-0). Influence of Phase Composition of Bulk Tungsten Vanadium Oxides on the Aerobic Transformation of Methanol and Glycerol. European Journal of Inorganic Chemistry. 10:1204-1211. https://doi.org/10.1002/ejic.201800059

Influence of phase composition of bulk tungsten-vanadium oxides on the one-pot synthesis of acrylic acid from glycerol

Daniel Delgado [1], Alessandro Chieregato [1,2], M. Dolores Soriano [1], E. Rodríguez-Aguado [3], Lidia Ruiz-Rodríguez [1], E. Rodriguez Castellon [3], Jose M. Lopez Nieto[1, *]

1) Instituto de Tecnología Química, Universitat Politècnica de València-Consejo Superior de Investigaciones Científicas, Avenida de los Naranjos s/n, 46022 Valencia, Spain. E-mail: jmlopez@itq.upv.es
2) Current affiliation: Total Research & Technology, R&D Department of Catalysis for Refining and Base Chemicals, Zone Industrielle Feluy C, B-7181 Seneffe, Belgium.
3) Departamento de Química Inorgánica, Facultad de Ciencias, Universidad de Málaga, 29071 Málaga, Spain

Abstract

A series of W-V-O catalysts which present different m-WO_3 and h-WO_3 phase contents were hydrothermally synthesized employing different tungsten, vanadium and ammonium precursors. Characterization of these materials was carried out by several physicochemical techniques such as powder X-Ray diffraction, N_2-adsorption, SEM, XEDS, TG, Raman, FT-IR spectroscopy, TPD-NH_3 and XPS. Finally, acid-redox properties were analyzed using methanol aerobic transformation as a characterization reaction. A correlation between phase composition as well as acid- and redox- properties was observed, which were correlated to the catalytic performance of the titled materials in the one-pot glycerol oxydehydration reaction. The m-WO_3 phase shows a concentration of acid sites significantly lower than that of h-WO_3, making acidity directly related to the presence of h-WO_3 crystals in the samples, which is fundamental in order to attain high selectivity to both acrolein and acrylic acid during the one-pot glycerol oxydehydration. Also, V-sites in h-WO_3 present higher selectivity in the consecutive reaction (acrolein partial oxidation to acrylic acid), while V-sites in m-WO_3 phase fundamentally lead to the formation of carbon oxides.

Keywords: Glycerol, Acrylic acid, Oxidehydration, W–V mixed oxides, Hexagonal tungsten bronze

1. INTRODUCTION

Tungsten oxides have received special attention in the last decades since they present potential uses in a wide variety of fields such as electrochromic displays, gas sensing, superconductivity or catalysis.[1-4] Particularly, they have emerged in the last years as interesting materials for several catalytic applications. Indeed, they are well-known multi-functional materials for fuel cells, being employed as electrocatalysts and supports.[5-8] Oxygen deficient tungsten oxides-based materials, known as tungsten bronzes, are known as catalysts for the electrochemical oxidation of C_2-C_3 alcohols [9-11] and hydrogen in acid media.[12] Tungsten bronzes have also been used in electrocatalysts for oxygen reduction, [13] photocatalysts [14] and as efficient catalysts in the hydrogenation of linear and cyclic alkenes, nitroarenes or unsaturated organosulfur compounds.[15] Moreover, they have been widely studied as acid catalysts for different processes,[16, 17] but also as acid-redox multifunctional materials, due to their ability to accommodate different kinds of metals and non-metals within the structure. Recently, mixed metal oxides with tetragonal tungsten bronze (TTB) structure have shown high activity and selectivity for the gas phase partial oxidation of olefins,[18] whereas materials presenting hexagonal tungsten bronze (HTB) structures have been proposed as active and selective catalysts in the aerobic transformation of alcohols, such as the one-pot oxydehydration of glycerol to acrylic acid.[19, 20] In this way, a parallelism between the selectivity to acrylic acid from glycerol and the catalytic behavior of the corresponding catalysts during the aerobic transformation of methanol was proposed.[21]

From the synthetic point of view, the control of key parameters of the synthesis, such as pH, organic additives or the precursors used on the formulation, made it possible to obtain different phase compositions, particles sizes and crystal shapes.

It was demonstrated that all these features can have an important influence in their functionality, specifically in their catalytic performance.[22-25]

Herein, we report on the preparation and characterization of a series of W-V-O materials and their catalytic behavior in the oxidation of methanol and the oxydehydration of glycerol. Depending on the W-, V- or ammonium-precursors, different morphologies, thermal stabilities and ratios of m-WO_3/h-WO_3 phases were obtained. The analysis of the selectivity profiles in the aerobic transformation of methanol sheds light on the acid-redox properties of the materials, which appear to be correlated with the m-WO_3/h-WO_3 phase ratio. In order to corroborate these findings, catalysts were finally tested in the glycerol oxydehydration reaction, where both acid and redox sites are necessary to achieve a relatively high yield to acrylic acid. It was found that the presence of h-WO_3 is pivotal to tune the acid- and redox- properties for the selective transformation of glycerol to acrylic acid.

2. EXPERIMENTAL

2.1. Synthesis of W-V-O oxides

Preparation of W-V-O materials was carried out under hydrothermal conditions from gels containing different tungsten, vanadium and ammonium precursors, while maintaining a constant W/V ratio of 1/0.3 in the synthesis gel (Table 1). Gels were obtained from aqueous solutions of the corresponding metal- (W- and V-) and ammonium-precursors: ammonium metatungstate hydrate (≥85 wt% WO_3 basis, Sigma–Aldrich), tungstic acid (99%, Sigma Aldrich), vanadium(IV) oxide sulfate hydrate (≥97%, Sigma–Aldrich), vanadyl acetylacetonate (99.98%, Sigma–Aldrich), ammonium chloride (99.998%,

Sigma–Aldrich), ammonium sulfate (99.0 %, Sigma–Aldrich), ammonium acetate (98%, Sigma–Aldrich) or aqueous ammonia (25 %, Panreac). These materials will be named as **AMT**-series or **TA**-series, depending on the tungsten precursors, i.e. ammonium metatungstate or tungstic acid, respectively.

The synthesis gels were introduced in Teflon-lined stainless steel autoclaves, under N_2 atmosphere (1 bar), and treated at 175 ºC for 48h. The resulting solids were then filtered, washed with water, and dried at 100 ºC overnight. Finally, heat-treatment was carried out in two steps: i) a heat-treatment at 200ºC for 1 h, in air flow, and ii) a heat-treatment at 600 ºC for 2 h under N_2 flow (15 mL min^{-1} g^{-1}).

2.2. Characterization of catalysts

Powder X-Ray diffraction (XRD) patterns were collected in a PANalytical X'Pert PRO diffractometer equipped with and X´Celerator detector in a Bragg-Brentano geometry using Kα radiation of copper.

Surface areas were calculated by BET method, from adsorption isotherms recorded on a Micromeritics ASAP 2000. Solids were degassed previously under vacuum at 400ºC.

X-Ray energy-dispersive spectroscopy (XEDS) analyses were performed using an Oxford LINK ISIS system connected to a JEOL 6300 electron microscope with the SEMQUANT program, which introduces ZAF correction. The counting time for each analysis was 100s.

Scanning electron microscopy (SEM) micrographs were carried out in a field emission ZEISS Ultra-55 scanning electron microscope operating at an accelerating voltage of 2 kV.

Raman spectra were collected with an inVia Renishaw spectrometer using an exciting wavelength of 514 nm. The laser used was a Renishaw HPNIR with an approximate power on the samples of about 15 Mw.

Thermogravimetric experiments were carried out in a Mettler-Toledo TGA/SDTA 851 thermobalance. Approximately 10 mg of sample were heated at 600 ºC at 10ºC/min heating rate in a 50 mL/min synthetic air flow.

Infrared spectra in the 400-4000 cm^{-1} region were acquired at room temperature with a Nicolet 205xB spectrophotometer at a spectral resolution of 1 cm^{-1} and 128 accumulations per scan.

X-ray photoelectron spectra were registered using a Physical Electronics PHI 5700 spectrometer with non-monochromatic MgKα radiation (300 W, 15 kV, and 1256.6 eV) with a multi-channel detector. Spectra of powder samples were recorded in the constant pass energy mode at 29.35 eV, using a 720 μm diameter analysis area. Charge referencing was measured against adventitious carbon (C 1*s* at 284.8 eV). A short acquisition time of 10 min was first used to examine C 1*s*, V 2*p* regions to avoid photoreduction of vanadium(V) species. A PHI ACCESS ESCA-V6.0 F software package was used for acquisition and data analysis. A Shirley-type background was subtracted from the signals. Recorded spectra were always fitted using Gaussian–Lorentzian curves in order to determine the binding energies of the different element core levels more accurately.

Temperature programmed desorption of ammonia (NH_3-TPD) was carried out to evaluate the total acidity of the catalysts. Prior to the adsorption of NH_3, 80 mg of each sample were heated from room temperature to 500ºC (heating rate: 10 ºC min^{-1}) and then maintained at 500ºC during 10 min under flowing He (35 mL min^{-1}). Subsequently, samples were cooled to 10ºC and then exposed to flowing pure ammonia for 5 min. With

the aim to remove the physisorbed ammonia, samples were cleaned using He flow (35 mL min^{-1}) again. NH_3-TPD was performed between 100ºC and 500ºC with a heating rate of 10ºC min^{-1} by using a helium flow and maintained at 500ºC for 15 min. The desorbed ammonia was analyzed by online gas chromatography (Shimadzu GC-14A) provided with a TCD.

2.3. Reactivity tests

The aerobic transformation of methanol was carried out in a fixed bed reactor in the 180-380 ºC temperature range, at atmospheric pressure and a contact time, W/F, of 6.8 g_{CAT} h $(mol_{CH3OH})^{-1}$. The feed consisted of methanol/oxygen/nitrogen with a molar ratio of 6/13/81. Analysis of reactants and reaction products was performed by means of gas chromatography using two different chromatographic columns: i) Molecular sieve 5 Å (3m length); and ii) RT-U bond (30 m, 0.53 i.d.).

The catalytic tests for the phase glycerol oxidehydration were also conducted in a fixed-bed reactor at atmospheric pressure, with the following reaction mixture: 2 mol% glycerol, 40 mol% water, 4 mol% oxygen and 54 mol% helium, and a contact time W/F of 81 g_{CAT} h $(mol_{GLY})^{-1}$. The effluent stream was bubbled through a condenser, which was refrigerated at 0-3 ºC. The remaining gaseous stream containing carbon oxides and oxygen was analyzed by an online gas chromatograph equipped with: (i) molecular sieve 5Å (3 m); and (ii) Porapak Q (3 m). The condensed aqueous solution containing all the reaction products and the unconverted glycerol was analyzed by gas chromatography using a Varian 3900 chromatograph equipped with a 100% dimethylpolysiloxane capillary column (100 m x 0.25 mm x 0.5).

4. RESULTS AND DISCUSSION

4.1. Characterization of W-V-O metal oxides

The main physical and chemical features of W-V-O materials are summarized in Table 1. V/(W+V) ratios after synthesis are in the range between 0.12-0.18 for all the studied materials. This means that almost half of the vanadium added into the synthesis gel (W/V ratio in the synthesis of 1/0.3) does not incorporate into the oxides frame after hydrothermal treatment, regardless the type of precursor used for the preparation.

Figure 1 shows XRD patterns of both as-prepared (Fig. 1A) and heat-treated materials (Fig. 1B). Focusing on as-prepared catalysts, two pure bronze phases where obtained when ammonium metatungstate or an ammonia/ammonium chloride mixture were used as ammonium source (Fig. 1A, patterns a to c). Characteristic diffraction patterns of these phases correspond to those of an hexagonal tungsten bronze type structure (h-WO_3) (JCPDS: 85-2460) (Fig. 1A, patterns a and c),[19, 26] and a pseudo-crystalline phase related to the ReO_3-phase, with long-range order just along c-axis (Fig. 1A, pattern b).[20] On the other hand, when using tungstic acid and other ammonium salts as precursors, mixtures of h-WO_3 and perovskite related ReO_3-type monoclinic WO_3 phase (m-WO_3) were obtained (JCPDS: 43-1035) (Fig. 1A, patterns d-g). An unknown crystalline phase was also formed when using ammonium acetate, tungstic acid and vanadyl acetylacetonate on the synthesis (Fig. 1A, pattern g), which decomposes after heat-treatment (Fig. 1B, pattern g). In this regard, the presence of meta-tungstate in the synthesis gel, or even the possible in-situ formation of isopolytungstates during the hydrothermal treatment could have an important influence in the formation of pure bronze-type compounds.[18, 27, 28] XRD patterns of heat-treated materials are presented in Fig. 1B. It can be seen that as-prepared pure h-WO_3 phases remain stable after the thermal treatment (Fig. 1B, patterns a and c). However, in the remaining cases bronze-type phases partially decompose into m-WO_3

(Fig. 1B, patterns b, d-e). Relative proportions of h-WO_3 phase in the samples were estimated from the intensities of (100) and (022) Bragg peaks of h-WO_3 and m-WO_3 phases, respectively (Table 1). As-prepared materials present h-WO_3 phase percentages in the range 41-100 %, while after heat-treatment percentages in the range 0-100 % were obtained, due to bronze phase partial or total decomposition (Table 1). Moreover, catalysts presenting higher percentages of bronze phase also present higher surface areas (Table 1).

Figure 2 shows SEM micrographs of as-prepared materials. Pure h-WO_3 and pseudocrystalline phases present mainly 1D morphologies, such as rod and needle-shaped structures (Fig. 2, a-c). On the other hand, samples consisting of h-WO_3/m-WO_3 mixtures present both block-shaped and rod/ needle-shaped structures (Fig. 2, d-g). This fact could have an important influence in the stability of the tungsten bronze phases since block-shaped morphologies exposing higher proportion of (001) faces could facilitate the elimination of NH_4^+ cations through the channels, favoring phase transitions to m-WO_3 type structures.[29, 30] Moreover, it can be noted that after heat treatment block-type particles undergo decomposition into platelet-shaped ones, which has been identified with m-WO_3 type structure (Fig. 3a). However, 1D morphologies retain their shape after heat-treatment (Fig. 3b). According to XRD patterns, and other results reported previously in literature, these morphologies can be attributed to tungsten bronze-type structures.[31-33] Therefore, heat-treated catalyst, which present a mixture of both tungsten-bronze and m-WO_3 phases, show both 1D structures and platelet-shaped particles (Fig. 3c). Nevertheless, we cannot exclude the influence of the effective substitution of V for W within h-WO_3 framework, which has also been reported to increase the thermal stability of the hexagonal tungsten bronze structure.[21]

Raman spectra of heat-treated samples that present different h-WO_3/m-WO_3 ratio are depicted in Figure 4. They show typical Raman profiles for tungsten based oxides at ca. 709, 808 and 969 cm^{-1}, that can be assigned to W-O-V, W-O-W and M=O (M: W, V) bond vibrations respectively.[34-36] It is noteworthy to mention that no bands over 1000 cm^{-1} are found on the spectra, which means that no V_2O_5 was formed after calcination.[37] Pure monoclinic WO_3 phase material presents Raman bands centered at 709, 808 and 983 cm^{-1} (Fig. 4, spectrum f), while a slight shift to lower frequencies occurs on the pure HTB phase, with corresponding Raman signals at 683, 800 and 969 cm^{-1} respectively (Fig. 4, spectrum a). Furthermore, the presence of both h-WO_3 and m-WO_3 phases gives rise to a Raman spectrum showing characteristic bands from both of them (Fig. 4, spectra d-e and g).

Figure 5 presents Differential Thermogravimetric (DTG) curves of as-prepared materials. DTG profiles show two main weight losses in the temperature ranges already reported for other tungsten oxide-based materials: i) below 200 ºC; and ii) in the range 250-450 ºC, which have been assigned to the elimination of physisorbed water and ammonium cations from the channels respectively.[38, 39] These weight losses are notably higher in samples with high proportion of h-WO_3 or pseudocrystalline phase (Table 1), which also present a weight gain around 500 ºC, fact that could be associated to the oxidation of V^{4+} and/or W^{+5} centers to V^{5+} and W^{6+}, respectively (Fig. 5, patterns a-c). In this way, an additional weight loss is also observed at 400 ºC in sample **TA-5**, that could be related to the previously mentioned unknown phase found by XRD (Fig. 5, pattern g).

FTIR spectra of as-prepared and heat-treated materials were collected in order to study the activation process of the catalysts (Fig. 6). As-prepared materials present three main bands in the range 3700-3000 cm^{-1} (Fig. 6A). The signal centered at 3430 cm^{-1} has been attributed to O-H groups stretching vibrations, while remaining signals appearing at 3215

and 3144 cm^{-1} are associated to N-H stretching vibrations of the corresponding ammonium cations located inside the channels.[38, 40, 41] However, heat-treated samples show no bands in the NH_4^+ region due to the elimination of these ions from the structure (Fig. 6B). The substitution of H^+ for ammonium ions within the channels has been reported to be the origin of the acid centers in tungsten bronze-type structure-based catalysts.[42]

Acid features of heat-treated materials were studied by means of temperature programmed desorption of ammonia (Fig. 7). It can be noted that the highest concentration of acid sites is obtained for high contents of bronze-type phases, either h-WO_3 or pseudocrystalline phase (Table 1). Thus, this suggest that the presence of relatively wider channels could favor the formation of Brönsted acid sites, by elimination of NH_4^+ ions during the activation at high temperature as reported elsewhere, meanwhile m-WO_3 structure would present a lower concentration of surface acid sites. Despite this, the influence of other variables, such as surface area or surface vanadium concentration cannot be ruled out. In fact, XPS experiments show very different vanadium surface contents (much lower than that of bulk composition in some cases) depending on the synthesis procedure (Table 1).

The V $2p_{3/2}$ core level spectra of all the studied W-V-O mixed oxide catalysis shows a single peak at 517.1-517.6 eV assigned to the presence of V(V), except in the case of sample AMT-1 were two contributions at 517.1 eV (86%) and 515.7 eV (14%) assigned to V(V) and V(IV) are observed, respectively (Fig. S1). The W 4*f* core level spectra for the studied catalysts are very similar, with a W $4f_{7/2}$ peak centered at 35.9-36.3 eV, assigned to W(VI) (Fig. S2).[43]

4.2. Catalytic results in the aerobic transformation of methanol

Methanol transformation has been widely used as a test reaction, either for determining acid and/or redox features, or for the elucidation of surface structure-reactivity relationships of bulk metal oxide catalysts.[44-46] Indeed, the selective transformation of methanol in aerobic conditions has been reported to be an efficient method to estimate acid/redox multifunctional properties in tungsten bronze-based catalysts.[21, 47] When a molecule of methanol reacts with Brönsted acid sites, it essentially leads to the formation of dimethyl ether (DME). On the other hand, when the reaction takes place on redox sites (e.g., $V^{4+/5+}$ sites) it leads to the formation of partial oxidation products, mainly formaldehyde (FA), and other oxygenates that form in minor amounts, such as methyl formiate (MF), dimethoxymethane (DMM) and carbon oxides (CO_x).[45]

Acid/redox features of W-V-O oxides were evaluated taking into account the selectivity profiles (Fig. 8) obtained for the different materials at low methanol conversion (c.a. 10%) (Fig. 9). Hence, selectivity to dimethyl ether, DME, progressively increases with the h-WO_3 phase concentration in the catalysts (Fig. 8, DME), while the opposite trend is observed in the production of partial oxidation products, i.e. DMM+MF+FA (grouped as "POPs"), in which the lower formation of HTB phase, the higher productivity is achieved (Fig. 8, POPs). Indeed, a clear relationship exists between h-WO_3/m-WO_3 ratio and acid redox properties of the samples, which is shown in Figure 9. As the m-WO_3 concentration increases in the catalysts, the acid function is progressively lost, for the benefit of the redox one, achieving almost total selectivity to POP´s in the absence of h-WO_3 phase. On the other hand, the presence of h-WO_3 phase leads to multifunctional acid/redox catalysts, in which its acid character increases with the concentration of bronze phase, achieving a maximum DME selectivity of c.a. 50 %. In the case of sample AMT-2 in which a pseudocrystalline phase is observed, the selectivity to POP´s and DME corresponds to

materials presenting ca. 88 % of h-WO_3 phase. In fact, XRD pattern shows a slight decomposition of this phase into m-WO_3 after the heat-treatment (Fig. 1B, pattern b).

4.2. Catalytic results in the oxydehydration of glycerol.

Tungsten and molybdenum/vanadium-based bronze phases have been reported to be one of the best catalytic systems for the production of acrolein (AC) and acrylic acid (AA) from glycerol.[19, 20, 47-51] In this regard the acid-redox character of the catalysts is pivotal. Acrolein is obtained by the direct dehydration of glycerol on acid sites of moderated strength, while acrylic acid (AA) is generated in a consecutive step by partial oxidation of acrolein on redox sites. In fact, the presence of $V^{+4/+5}$ and $Mo^{5+/6+}$ species within the crystal structure gives rise to the redox function in these materials (likely O^{2-} sites, as typically observed for redox oxides).[52] Therefore, the presence of a bifunctional acid-redox catalyst, in which both functions work at the same temperatures is necessary in order to obtain acrylic acid in a one-pot reaction system. Figure 10 shows the effect of HTB phase-content (in %) on the selectivity to both acrolein and acrylic acid (AA+AC) and CO_x, and the acrylic acid/acrolein ratio. As it can be seen, the increment of h-WO_3 % promotes the formation of both acrolein and acrylic acid. In fact, low amounts of h-WO_3 phase in the catalyst give rise to the formation of higher amounts of carbon oxides, rather than acrylic acid. Moreover, the AA/AC ratio increases with h-WO_3 content in the catalysts. These observations not only mean that vanadium sites in a m-WO_3 structure are not selective in the partial oxidation of acrolein to acrylic acid, but also that its low acidity (as it can be inferred from methanol aerobic transformation results) give rise to low selectivity to acrolein in the first reaction step and, accordingly, to low acrylic acid yields.

5. CONCLUSIONS

Several W-V-O catalysts presenting different proportions of h-WO_3 and m-WO_3 phases have been synthesized. Selecting the appropriate tungsten, vanadium and ammonium precursors, materials with different morphologies and thermal stability can be obtained. Indeed, block-shaped crystals undergo a higher thermal decomposition of the initial h-WO_3 phase into m-WO_3, while bronze-type phases, presenting 1D-Type morphologies (mainly rod and needle-shaped), show higher stability under the same thermal treatment. Catalytic tests on the aerobic transformation of methanol show that pure m-WO_3-type phase presents very low concentration of acid sites, showing mainly redox sites (selectivity to POP´s of c.a. 98 %). As h-WO_3 phase proportion increases, acid function is progressively generated, as it can be inferred from the selectivity profiles that show increasing amounts of DME, reaching approximately 50 % of selectivity to both POP´s and DME. Catalytic tests on glycerol oxydehydration reaction indicate that the absence of acid sites in m-WO_3 type phases has a negative effect in the production of acrolein and, accordingly, in the production of acrylic acid. The presence of h-WO_3 phase containing both acid and redox sites working in a cooperative way increases the production of acrolein in the first step and acrylic acid in the consecutive reaction. Moreover, acrylic acid/acrolein ratio increases with the h-WO_3 proportion, which means that V-sites into the bronze structure are selective to the partial oxidation of acrolein to acrylic acid, and also that redox sites in m-WO_3-type phase are less selective in the partial oxidation, producing essentially carbon oxides.

Acknowledgments

The authors acknowledge the DGICYT in Spain CTQ2012-37925-C03-2, CTQ2015-68951-C3-1-R, CTQ2015-68951-C3-3-R. Authors from ITQ also thank Project SEV-2016-0683 for financial support. D.D. thanks MINECO and Severo Ochoa Excellence Program for his fellowship (SVP-2014-068669). Authors also thank the Electron Microscopy Service of Universitat Politècnica de València for their support.

References

1. J. D. Guo and M. S. Whittingham, *Int. J. Mod. Phys. B*, 1993, **7**, 4145-4164.
2. H. Long, W. Zeng and H. Zhang, *J. Mater. Sci.: Mater. Electron.*, 2015, **26**, 4698-4707.
3. N. Haldolaarachchige, Q. Gibson, J. Krizan and R. J. Cava, *Phys. Rev. B: Condens. Matter Mater. Phys.*, 2014, **89**, 104520/104521-104520/104526.
4. Z.-F. Huang, J. Song, L. Pan, X. Zhang, L. Wang and J.-J. Zou, *Adv. Mater.*, 2015, **27**, 5309-5327.
5. T. Maiyalagan and B. Viswanathan, *J. Power Sources*, 2008, **175**, 789-793.
6. a) M. F. Weber, A. J. Bevolo, H. R. Shanks and G. C. Danielson, *J. Electrochem. Soc.*, 1981, **128**, 996-1003; b) B. Wickman, M. Wesselmark, C. Lagergren and G. Lindbergh, *Electrochim. Acta*, 2011, **56**, 9496-9503.
7. K.R. Dey, T. Debnath, C.H. Rüscher, M. Sundberg, A. Hussain, *J. Mater. Sci.*, 2011, **46**, 1388–1395.
8. Z. Zhang, J. Liu, J. Gu, L. Su and L. Cheng, *Energy Environ. Sci.*, 2014, **7**, 2535-2558.
9. M. Murawska, J. A. Cox and K. Miecznikowski, *J. Solid State Electrochem.*, 2014, **18**, 3003-3010.
10. X. P. Li, X. D. Xiang, H. Y. Yang, X. J. Wang, C. L. Tan and W. S. Li, *Fuel Cells*, 2013, **13**, 314-318.
11. P. J. Kulesza, I. S. Pieta, I. A. Rutkowska, A. Wadas, D. Marks, K. Klak, L. Stobinski and J. A. Cox, *Electrochim. Acta*, 2013, **110**, 474-483.
12. B. Broyde, *J. Catal.*, 1968, **10**, 13-18.
13. G. Li, Ch. Guo, M. Yan and S. Liu, *Appl. Catal. B: Environ.*, 2016, **183**, 142-148.
14. a) Y. Xi, Z. Chen, V. Gan Wei Kiat, L. Huang and H. Cheng, *Phys. Chem. Chem. Phys.*, 2015, **17**, 9698-9705; b) Y. Liu, S. Shrestha and W. E. Mustain, *ACS Catal.*, 2012, **2**, 456-463.
15. J. Song, Z.-F. Huang, L. Pan, J.-J. Zou, X. Zhang and L. Wang, *ACS Catal.*, 2015, **5**, 6594-6599.
16. K. Okumura, S. Ishida, R. Takahata and N. Katada, *Catal. Today*, 2013, **204**, 197-203.
17. C. Yue, X. Zhu, M. Rigutto and E. Hensen, *Appl. Catal., B*, 2015, **163**, 370-381.
18. P. Botella, B. Solsona, E. Garcia-Gonzalez, J. M. Gonzalez-Calbet and J. M. Lopez Nieto, *Chem. Commun.*, 2007, 5040-5042.
19. M. D. Soriano, P. Concepcion, J. M. Lopez Nieto, F. Cavani, S. Guidetti and C. Trevisanut, *Green Chem.*, 2011, **13**, 2954-2962.
20. A. Chieregato, M. D. Soriano, E. García-González, G. Puglia, F. Basile, P. Concepción, C. Bandinelli, J. M. López Nieto and F. Cavani, *ChemSusChem*, 2015, **8**, 398-406.
21. M. D. Soriano, A. Chieregato, S. Zamora, F. Basile, F. Cavani and J. M. Lopez Nieto, *Top. Catal.*, 2016, **59**, 178-185.

22. D. Nagy, D. Nagy, I. M. Szilagyi and X. Fan, *RSC Adv.*, 2016, **6**, 33743-33754.
23. S. Lin, Y. Guo, X. Li and Y. Liu, *Mater. Lett.*, 2015, **152**, 102-104.
24. B. Miao, W. Zeng, S. Hussain, Q. Mei, S. Xu, H. Zhang, Y. Li and T. Li, *Mater. Lett.*, 2015, **147**, 12-15.
25. A. C. Marques, L. Santos, M. N. Costa, J. M. Dantas, P. Duarte, A. Goncalves, R. Martins, C. A. Salgueiro and E. Fortunato, *Sci. Rep.*, 2015, **5**, 9910.
26. A. Magneli, *Acta Chem. Scand.*, 1953, **7**, 315-324.
27. C. D. Vanderpool, M. B. MacInnis and J. C. Patton, *Journal*, 1976.
28. M. Sanchez Sanchez, F. Girgsdies, M. Jastak, P. Kube, R. Schlögl and A. Trunschke, *Angew. Chem. Int. Ed.*, 2012, **51**, 7194-7197.
29. E. Garcia-Gonzalez, M. D. Soriano, E. Urones-Garrote and J. M. Lopez Nieto, *Dalton Trans.*, 2014, **43**, 14644-14652.
30. I. M. Szilágyi, J. Madarász, G. Pokol, P. Király, G. Tárkányi, S. Saukko, J. Mizsei, A. L. Tóth, A. Szabó and K. Varga-Josepovits, *Chem. Mater.*, 2008, **20**, 4116-4125.
31. C. Guo, S. Yin, P. Zhang, M. Yan, K. Adachi, T. Chonan and T. Sato, *J. Mater. Chem.*, 2010, **20**, 8227-8229.
32. P. Botella, E. García-González, J. M. López Nieto and J. M. González-Calbet, *Solid State Sci.*, 2005, **7**, 507-519.
33. Y. Kong, H. Sun, X. Zhao, B. Gao and W. Fan, *Appl. Catal., A*, 2015, **505**, 447-455.
34. P. Botella, B. Solsona, J. M. Lopez Nieto, P. Concepcion, J. L. Jorda and M. T. Domenech-Carbo, *Catal. Today*, 2010, **158**, 162-169.
35. W. P. Griffith and P. J. B. Lesniak, *J. Chem. Soc. (A)*, 1969, 1066-1071.
36. Z. Zheng, B. Yan, J. Zhang, Y. You, C. T. Lim, Z. Shen and T. Yu, *Adv. Mater.*, 2008, **20**, 352-356.
37. C. Sanchez, J. Livage and G. Lucazeau, *J. Raman Spectrosc.*, 1982, **12**, 68-72.
38. I. M. Szilagyi, J. Madarasz, G. Pokol, F. Hange, G. Szalontai, K. Varga-Josepovits and A. L. Toth, *J. Therm. Anal. Calorim.*, 2009, **97**, 11-18.
39. N. E. Fouad, A. K. H. Nohman, M. A. Mohamed and M. I. Zaki, *J. Anal. Appl. Pyrolysis*, 2000, **56**, 23-31.
40. L. Huo, H. Zhao, F. Mauvy, S. Fourcade, C. Labrugere, M. Pouchard and J.-C. Grenier, *Solid State Sci.*, 2004, **6**, 679-688.
41. D. Perra, N. Drenchev, K. Chakarova, M. G. Cutrufello and K. Hadjiivanov, *RSC Adv.*, 2014, **4**, 56183-56187.
42. K. Oshihara, T. Hisano and W. Ueda, *Top. Catal.*, 2001, **15**, 153-160.
43. J. R. Sohn and M. Y. Park, *Langmuir*, 1998, **14**, 6140-6145.
44. I. E. Wachs and K. Routray, *ACS Catal.*, 2012, **2**, 1235-1246.
45. J. M. Tatiboueet, *Appl. Catal., A*, 1997, **148**, 213-252.
46. M. Badlani and I. Wachs, *Catal. Lett.*, 2001, **75**, 137-149.
47. A. Chieregato, M. D. Soriano, F. Basile, G. Liosi, S. Zamora, P. Concepcion, F. Cavani and J. M. Lopez Nieto, *Appl. Catal., B*, 2014, **150-151**, 37-46.
48. K. Omata, K. Matsumoto, T. Murayama and W. Ueda, *Catal. Today*, 2016, **259**, 205-212.
49. A. Chieregato, F. Basile, P. Concepción, S. Guidetti, G. Liosi, M. D. Soriano, C. Trevisanut, F. Cavani and J. M. L. Nieto, *Catal. Today*, 2012, **197**, 58-65.
50. M. D. Soriano, A. Chieregato, S. Zamora, F. Basile, F. Cavani and J. M. López Nieto, *Top Catal*, 2015, **2-4**, 175-185.
51. Y. S. Yun, K. R. Lee, H. Park, T. Y. Kim, D. Yun, J. W. Han and J. Yi, *ACS Catal.*, 2015, **5**, 82-94.
52. F. Cavani, S. Albonetti, F. Basile, A. Gandini, *Chemicals and Fuels from Bio-Based Building Blocks*, Wiley-VCH Verlag GmbH & Co., 2016, DOI: 10.1002/9783527698202.

Table 1. Characteristics of W-V-O mixed oxides catalysts.

Sample	Precursors [a]			V/(W+V) atomic ratio		h-WO_3 phase content (%) [d]		S_{BET}	Weight loss at 350 ºC [e]	TPD-NH_3 [f]
	W	V	NH_4^+-salt	Bulk [b]	surface [c]	As-prepared	Heat-treated	(m^2/g)	(%)	(μmol/g)
AMT-1	AMT	VS	-	0.17	0.05	100	100	20.5	5.42	n.d.
AMT-2	AMT	VOAC	-	0.17	0.16	n.d.[g]	n.d.[g]	16.1	5.37	127
TA-1	TA	VS	NH_3(aq)/NH_4Cl	0.16	0.07	100	100	32.8	5.65	241
TA-2	TA	VS	NH_4SO_4	0.12	n.d.	42	31	13.5	2.58	n.d.
TA-3	TA	VS	NH_4Cl	0.12	0.08	46	26	7.2	1.77	50
TA-4	TA	VS	$NH_4CH_3CO_2$	0.17	0.15	41	0	7.9	2.91	86
TA-5	TA	VOAC	$NH_4CH_3CO_2$	0.18	0.19	60	54	26.6	4.82	88

a) **AMT**= $(NH_4)_6H_2W_{12}O_{40;}$ **TA**= H_2WO_4; **VS**= $VOSO_4$; **VOAC**= $VO(acac)_2$; b) W/V ratio obtained by X-Ray energy-dispersive spectroscopy (XEDS); c) Calculated by X-Ray Photoelectron Spectroscopy (XPS); d) Calculated from equation: HTB (%)= 100 x I_{100}(HTB)/[I_{022}(m-WO_3)+I_{100}(HTB)]; e) Obtained by thermogravimetric analysis; f) Temperature-programed desorption of ammonia; g) A Pseudocrystalline phase is only observed

Caption to figures

Fig. 1. XRD patterns of as-prepared (A) and heat-treated (B) W-V-O oxides: a) AMT-1; b) AMT-2; c) TA-1; d) TA-2; e) TA-3; f) TA-4; g) TA-5. Red: h-WO_3. Blue: m-WO_3.

Fig. 2. SEM micrographs of as-prepared oxides: a) AMT-1; b) AMT-2; c) TA-1; d) TA-2; e) TA-3; f) TA-4; g) TA-5.

Fig. 3. SEM and TEM micrographs of heat-treated materials. a) TA-4; b) AMT-1; c) TA-5.

Fig.4. Raman spectra of heat-treated W-V-O catalysts: a) AMT-1; b) AMT-2; c) TA-1; d) TA-2; e) TA-3; f) TA-4; g) TA-5.

Fig.5. Differential thermogravimetric profiles of as-prepared oxides: a) AMT-1; b) AMT-2; c) TA-1; d) TA-2; e) TA-3; f) TA-4; g) TA-5.

Fig.6. FTIR spectra of as-prepared (A) and heat-treated (B) catalysts: a) AMT-1; b) AMT-2; c) TA-1; d) TA-2; e) TA-3; f) TA-4; g) TA-5.

Fig. 7. TPD-NH_3 profiles of selected W-V-O materials: a) TA-4; b) TA-3; c) TA-5: d) AMT-2; e) TA-1.

Fig. 8. Selectivity to dimethyl ether (DME) (A) and selectivity to partial oxidation products (POP´s) (B) of W-V-O catalysts: AMT-1 (◀); AMT-2 (**x**); TA-1 (▷);TA-2 (▲); TA-3 (○);TA-4 (■);TA-5 (▽).

Fig. 9. Variation of the selectivity to DME (**red**) and to partial oxidation products, POP´s (**blue**), vs. the amount of h-WO_3 phase in W-V-O catalysts during the aerobic transformation of methanol on W-V-O oxides at a methanol conversion of 10 %: (●) AMT-1; (◘) on catalysts of TA-series. The amount of h-WO_3 phase as in Table 1. The

percentage of bronze phase of AMT-2 catalyst (**x**), has been calculate by considering the DME selectivity value achieved in this case.

Fig. 10. Variation of the selectivity to acrylic acid + acrolein (●) selectivity to CO_x (◘) and the acrylic acid / acrolein ratio (☆) as a function of the percentage of HTB-type phase during the glycerol oxidehydration over W-V-O materials. Reaction conditions: T= 320 ºC; Contact time, W/F, of 81 g_{CAT} h $(mol_{GLY})^{-1}$.

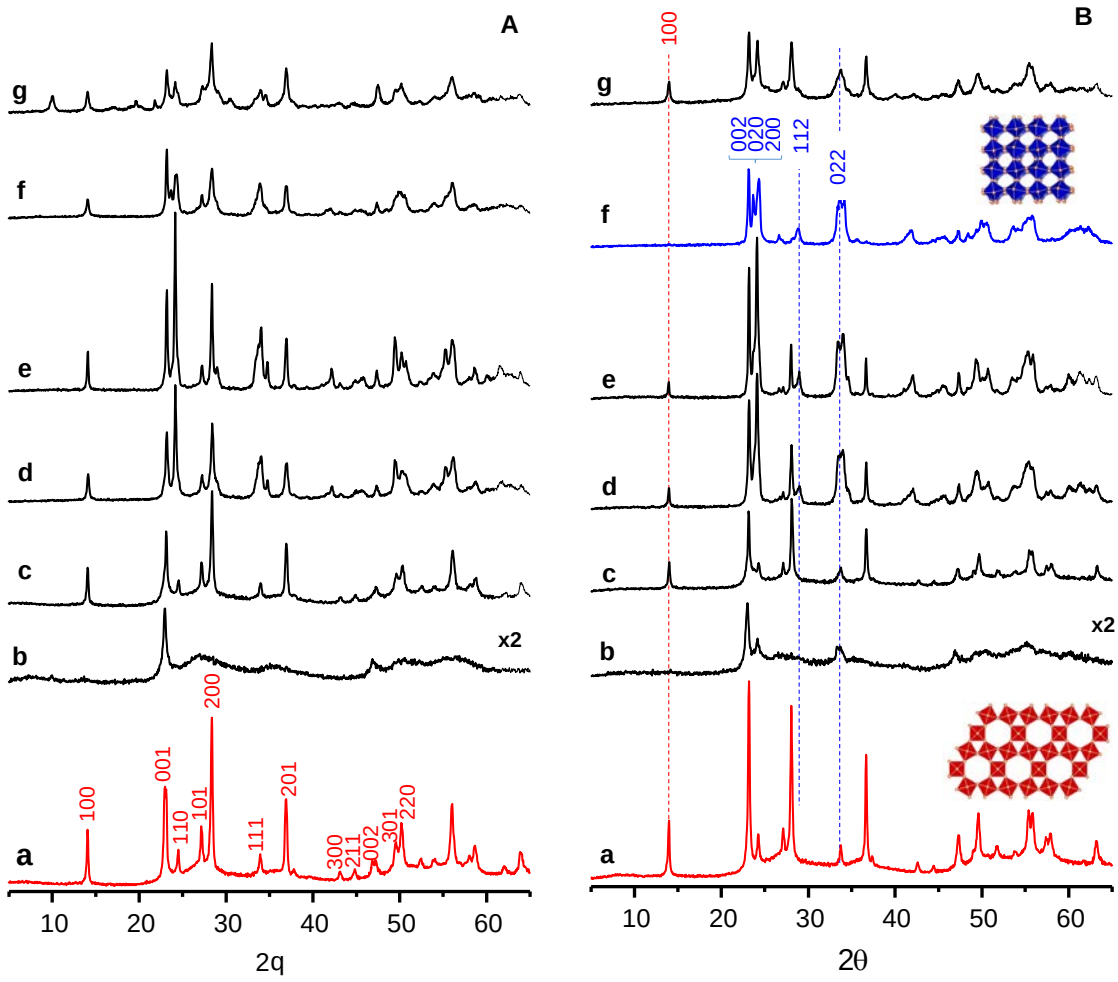
A
B
g
f
e
d
c
b
a
x2
100
001
110
101
200
111
201
300
211
002
301
220
002
020
200
112
022
10
20
30
40
50
60
2q
2θ

Figure 1

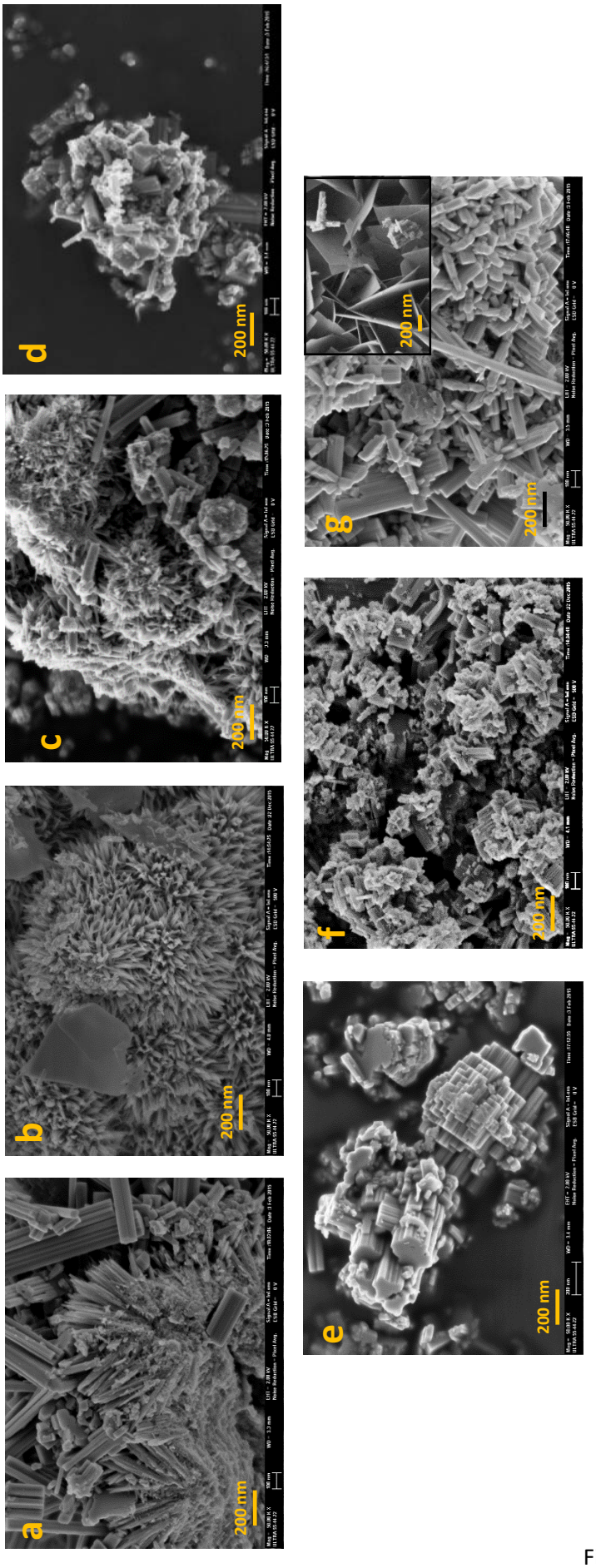

Figure 2

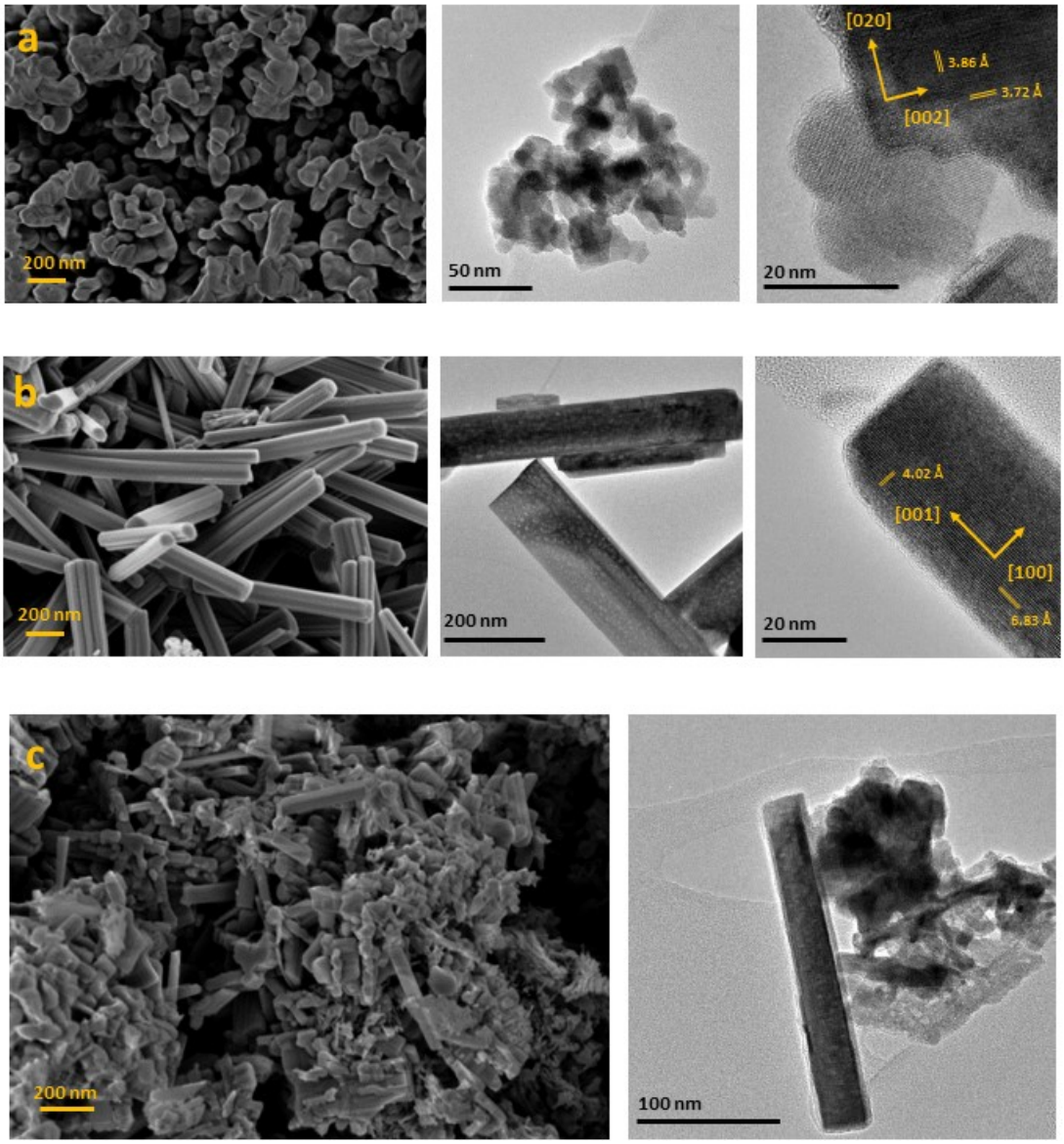
a
200 nm
50 nm
[020]
3.86 Å
3.72 Å
[002]
20 nm
b
200 nm
200 nm
4.02 Å
[001]
[100]
6.83 Å
20 nm
c
200 nm
100 nm

Figure 3

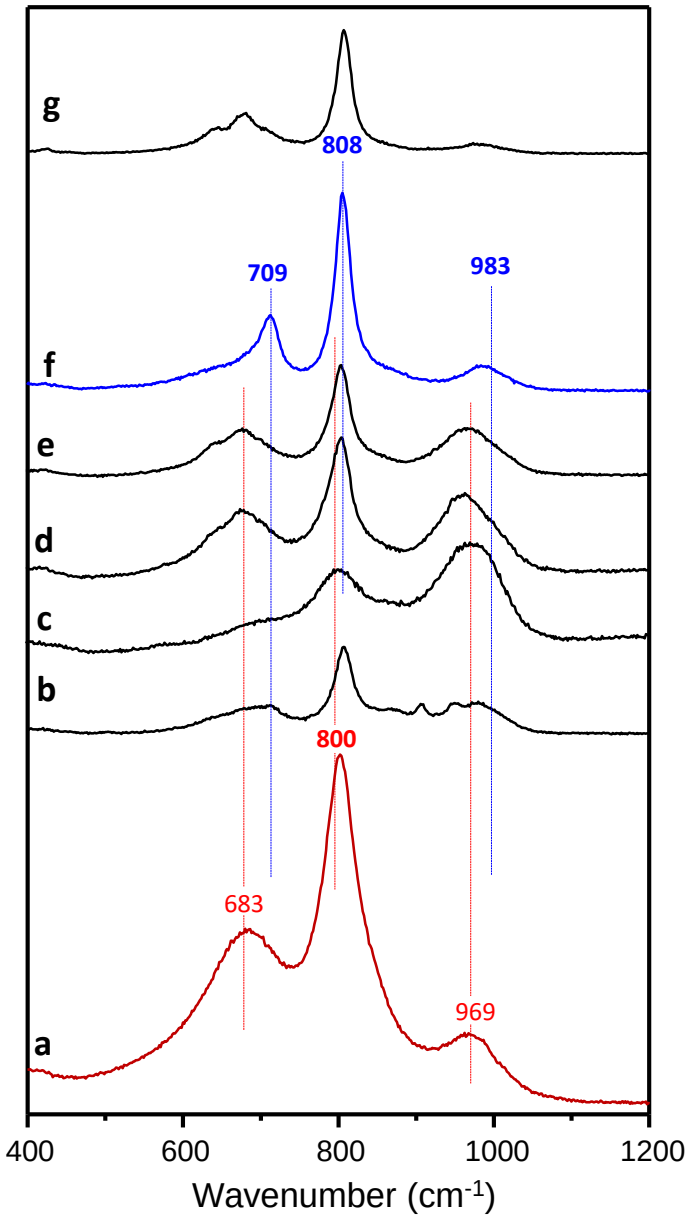
g
808
709
983
f
e
d
c
b
800
683
969
a
400
600
800
1000
1200
Wavenumber (cm-1)

Figure 4

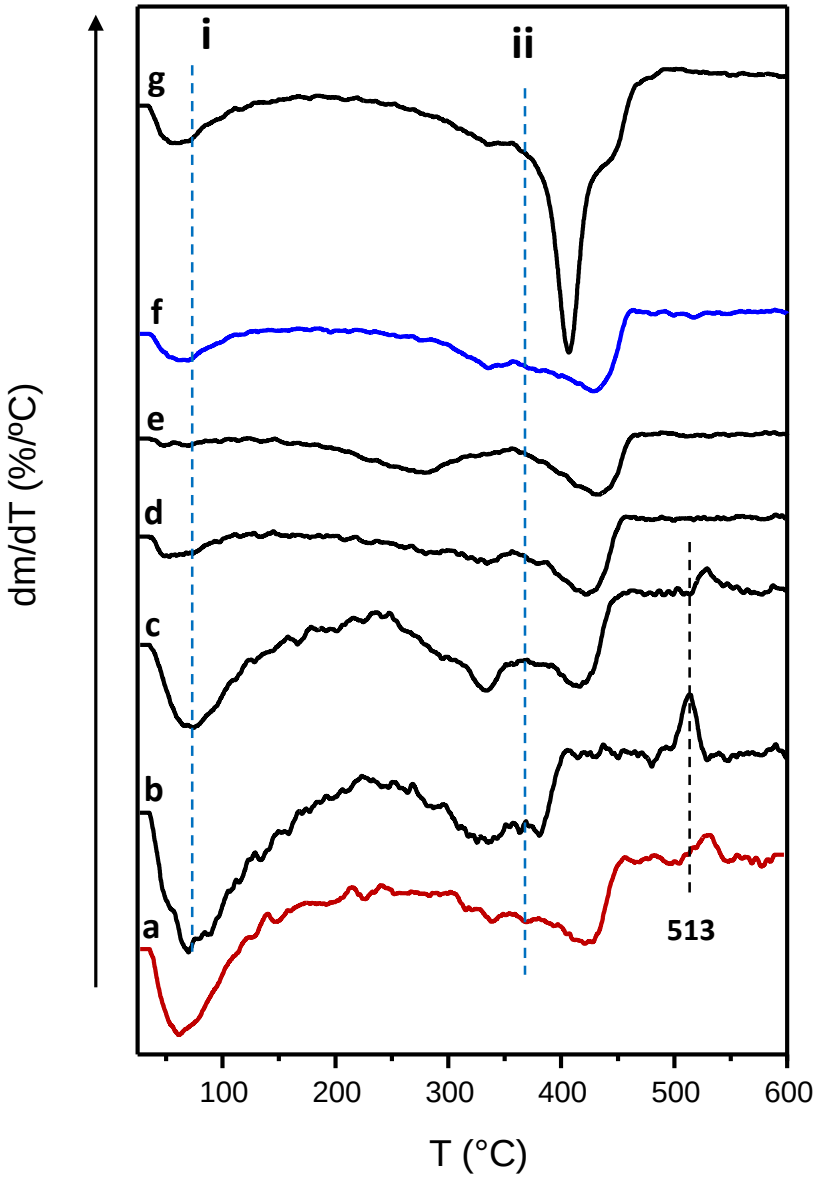

Figure 5

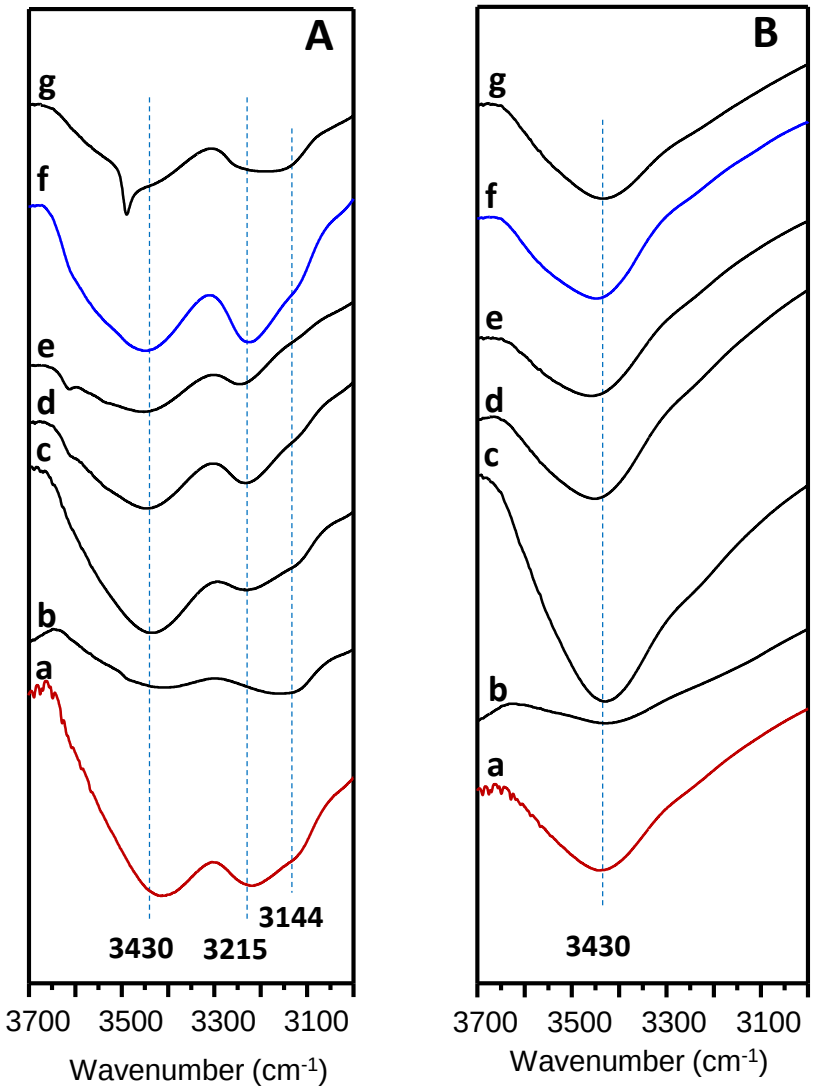
A
g
f
e
d
c
b
a
3144
3430
3215
3700
3500
3300
3100
Wavenumber (cm-1)
B
g
f
e
d
c
b
a
3430
3700
3500
3300
3100
Wavenumber (cm-1)

Figure 6

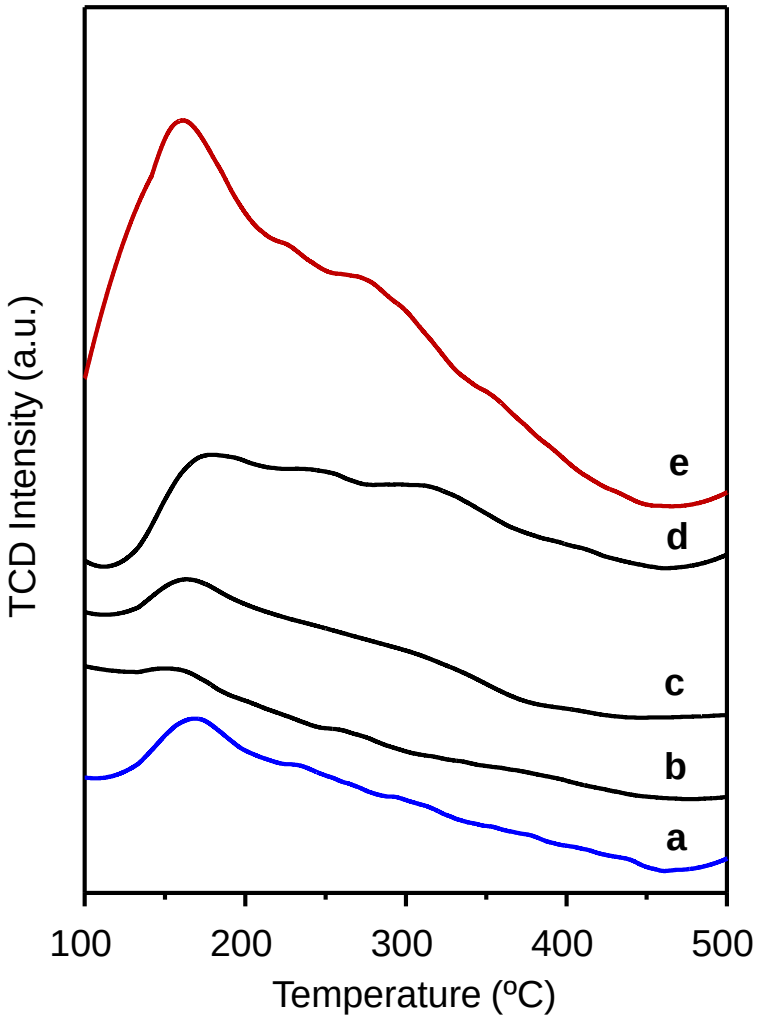

Figure 7

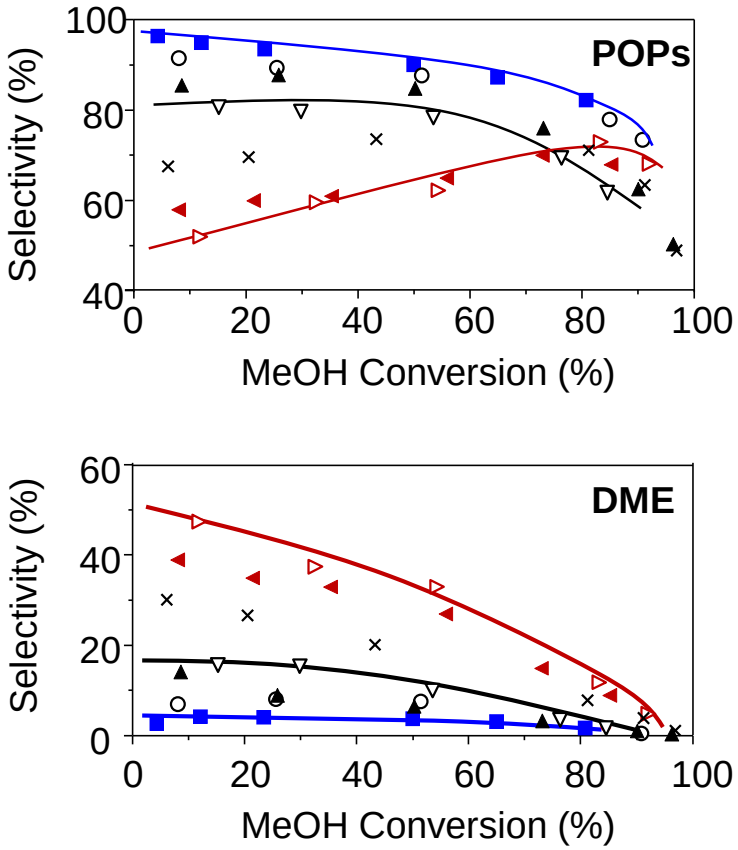
POPs
Selectivity (%)
MeOH Conversion (%)
DME
Selectivity (%)
MeOH Conversion (%)

Figure 8

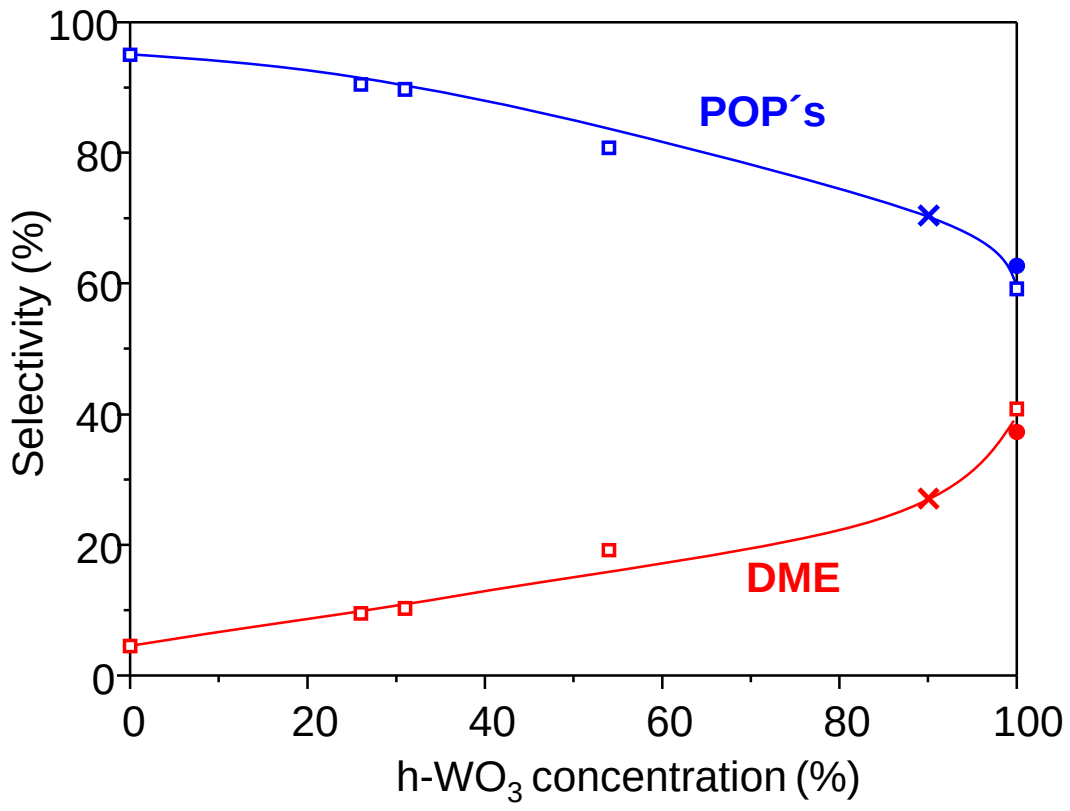
100
80
60
40
20
0
Selectivity (%)
POP´s
DME
0
20
40
60
80
100
h-WO3 concentration (%)

Figure 9

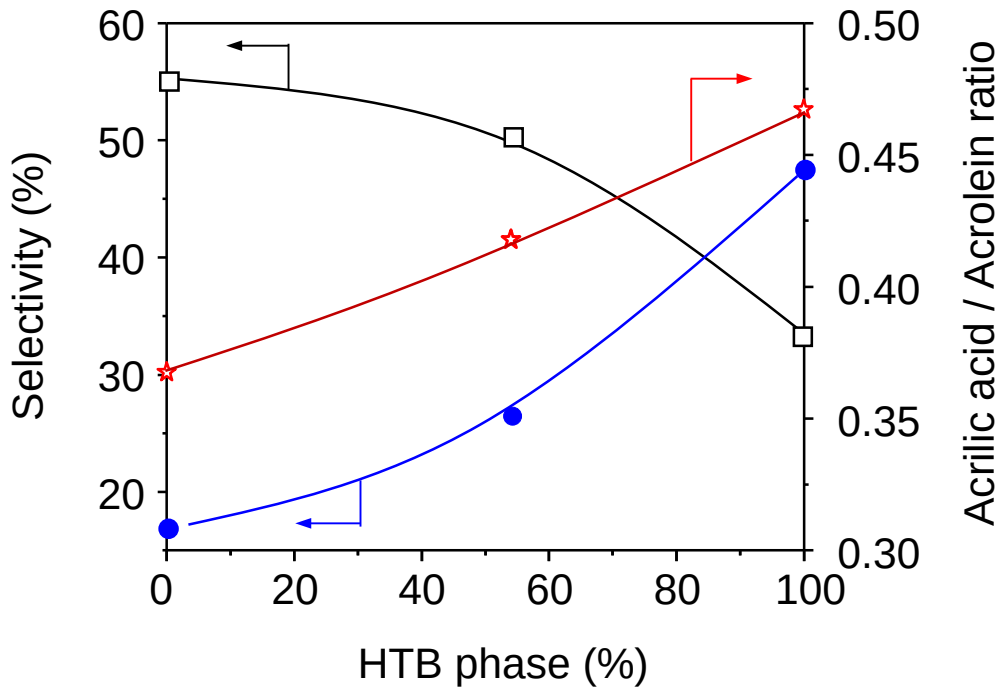
Selectivity (%)
Acrilic acid / Acrolein ratio
HTB phase (%)
60
50
40
30
20
0.50
0.45
0.40
0.35
0.30
0
20
40
60
80
100

Figure 10